2490 *Macromolecules* **2010**, *43*, 2490–2501
DOI: 10.1021/ma902714p

Macromolecules
ARTICLE

Thermoresponsive PS-*b*-PNIPAM-*b*-PS Micelles: Aggregation Behavior, Segmental Dynamics, and Thermal Response

Joseph Adelsberger,[†] Amit Kulkarni,[†] Abhinav Jain,[†] Weinan Wang,[†] Achille M. Bivigou-Koumba,[‡] Peter Busch,[§] Vitaliy Pipich,[§] Olaf Holderer,[§] Thomas Hellweg,[⊥] André Laschewsky,[‡] Peter Müller-Buschbaum,[†] and Christine M. Papadakis*,[†]

[†]*Physikdepartment E13, Technische Universität München, James-Franck-Str. 1, 85747 Garching, Germany,* [‡]*Institut für Chemie, Universität Potsdam, Karl-Liebknecht-Str. 24-25, 14476 Potsdam-Golm, Germany,* [§]*Forschungszentrum Jülich GmbH, Jülich Centre for Neutron Science at FRM II, Lichtenbergstr. 1, 85747 Garching, Germany, and* [⊥]*Physikalische Chemie I, Universität Bayreuth, Universitätsstr. 30, 95447 Bayreuth, Germany*

Received December 10, 2009; Revised Manuscript Received January 26, 2010

ABSTRACT: We have studied the thermal behavior of amphiphilic, symmetric triblock copolymers having short, deuterated polystyrene (PS) end blocks and a large poly(*N*-isopropylacrylamide) (PNIPAM) middle block exhibiting a lower critical solution temperature (LCST) in aqueous solution. A wide range of concentrations (0.1−300 mg/mL) is investigated using a number of analytical methods such as fluorescence correlation spectroscopy (FCS), turbidimetry, dynamic light scattering (DLS), small-angle neutron scattering (SANS), and neutron spin-echo spectroscopy (NSE). The critical micelle concentration is determined using FCS to be 1 μM or less. The collapse of the micelles at the LCST is investigated using turbidimetry and DLS and shows a weak dependence on the degree of polymerization of the PNIPAM block. SANS with contrast matching allows us to reveal the core−shell structure of the micelles as well as their correlation as a function of temperature. The segmental dynamics of the PNIPAM shell are studied as a function of temperature and are found to be faster in the collapsed state than in the swollen state. The mode detected has a linear dispersion in q^2 and is found to be faster in the collapsed state as compared to the swollen state. We attribute this result to the averaging over mobile and immobilized segments.

1. Introduction

"Smart" polymeric hydrogels have received increasing attention as they respond in a controlled and reversible way with a volume change to a weak external stimulus, such as temperature, light, electric or magnetic fields, or ionic strength.[1,2] Especially thermosensitive polymers are of great interest for medical and drug delivery applications, bioseparation, and diagnostics[3−5] as well as for porous membranes for molecular filtration where the permeability can be controlled by a change of temperature across the lower critical solution temperature (LCST).[6−8] Polymers with an LCST behavior, i.e., a temperature-dependent solubility in water, are attractive candidates because they are swollen below the LCST and collapsed, i.e., water-insoluble, above. A widely used LCST polymer is poly(*N*-isopropylacrylamide) (PNIPAM). In aqueous solution, its LCST at 32 °C is attributed to alterations in the hydrogen-bonding interactions of the amide group.[9−11] The LCST is almost independent of the PNIPAM molar mass and of concentration (up to 20 wt %), which has been attributed to sequential hydrogen bond formation between PNIPAM and H_2O.[12] So far, macroscopic gels,[13−15] microgels,[16−19] and core−shell particles with a cross-linked hydrophobic core and a cross-linked responsive shell[20−23] have been studied, and their collapse transitions have been characterized.

The hydrophobic modification of both ends of PNIPAM by alkyl end groups[24−26] or the use of block copolymers with one or two hydrophobic blocks and a PNIPAM block[8,27−36] are alternative routes to the formation of temperature-responsive micelles or micellar gels, where the ability to self-organize in aqueous solution is exploited. The effect of hydrophobic end groups on the LCST is discussed in detail in ref 36. Few previous investigations have focused on triblock copolymers with a PNIPAM middle block and polystyrene (PS) end blocks—the system considered by us in the present work. In all studies, the PS block was relatively large. In very dilute aqueous solution, flowerlike micelles were observed which collapse at the LCST of PNIPAM with the magnitude of the size decrease depending on the volume fraction of PNIPAM in the polymer.[31] PS-*b*-PNIPAM-*b*-PS triblock copolymers with high PNIPAM content and relatively large PS blocks (not directly soluble in water) were reported to take up large amounts of water upon immersion in water below the LCST.[8] Recently, the swelling of concentrated aqueous solutions of PS-*b*-PNIPAM-*b*-PS triblock copolymers forming the spherical and the bicontinuous morphology was investigated.[37] In the former, the PS blocks form spheres which are connected by PNIPAM blocks. During swelling, the PNIPAM blocks were observed to be strongly stretched. Moreover, the PS spheres were strongly deformed during the swelling process. However, in spite of the already published works, at present, no comprehensive data covering the structural and the dynamical aspects of such thermoresponsive systems are available over a broad range of concentrations.

In this work, we present an investigation of aqueous micellar solutions of ABA triblock copolymers consisting of a long PNIPAM middle block and two short PS end blocks that can

*Corresponding author: e-mail Christine.Papadakis@ph.tum.de; Ph +49 89 289 12 447; fax +49 89 289 12 473.

 Published on Web 02/11/2010

be directly dissolved in water. A wide range of concentrations (0.1−300 mg/mL) is studied to characterize the crossover between weakly and strongly correlated micelles. The micelle formation is investigated using fluorescence correlation spectroscopy (FCS). The behavior of these micelles at the LCST of PNIPAM is characterized using dynamic light scattering (DLS) with respect to the collapse of the micellar shell. The changes of the micellar structure and the correlation between micelles are investigated using small-angle neutron scattering (SANS). For the detailed and unambiguous SANS investigation, a strong scattering contrast between the core block, PS, and the thermoresponsive shell block is generated using fully deuterated PS blocks (P(S-d_8)) which are contrast-matched by D_2O. Alternatively, the PNIPAM block is contrast-matched by the appropriate D_2O/H_2O mixture, and selective information on the PS core is obtained. The synthesis of these polymers follows the previously reported synthesis of nondeuterated PS-*b*-PNIPAM-*b*-PS analogues.[34] Moreover, we have investigated the segmental dynamics of the PNIPAM blocks using neutron spin-echo spectroscopy on solutions and gels of the triblock copolymers. Again, the P(S-d_8) blocks are contrast-matched in D_2O, and the PNIPAM dynamics is investigated selectively. It is found to change drastically at the LCST.

In our study, we address the case of very short hydrophobic blocks [the PS (or P(S-d_8)) blocks have degrees of polymerization N_{PS} = 10 or 11] and very long PNIPAM blocks N_{PNIPAM} = 280−390. This block length ratio is expected to give better swelling ratios than the samples described in the literature.[8,31,37] Moreover, our polymers are directly soluble in water. Our previous investigations by turbidimetry and rheology show that they only form gels at high polymer concentration (30 wt %).[36] We attribute this behavior to the strong hydrophobicity of the PS blocks which results in lower bridging ratios than for less hydrophobic blocks.

Recently, we reported first results on the aggregation behavior of a P(S-d_8)$_{10}$-*b*-PNIPAM$_{390}$-*b*-P(S-d_8)$_{10}$ triblock copolymer, focusing on the structural changes at the collapse transition, determined using turbidimetry, dynamic light scattering (DLS), and small-angle neutron scattering.[35] In the present work, we specify these preliminary results on several triblock copolymers having different block lengths and having nondeuterated and deuterated PS blocks. Moreover, we give the critical micelle concentration found by FCS. The segmental dynamics of the PNIPAM block is investigated by means of NSE. The results will be compared to our previous investigations on other architectures, such as PS-*b*-PNIPAM diblock copolymers.[33,38]

The paper is structured as follows. After the Experimental Section, the synthesis and molecular characterization of P(S-d_8)-*b*-PNIPAM-*b*-P(S-d_8) are described. The micelle formation in dilute solution and the collapse transition of micellar solutions is discussed next. Then, the mesoscopic solution and gel structures are described. The segmental dynamics of the PNIPAM block and its changes at the collapse are described. Eventually, the results are summarized and compared to our previous results on a PS-*b*-PNIPAM diblock copolymer.

2. Experimental Section

2.1. Materials for Synthesis. Carbon disulfide [75-15-0] (99.9%, Acros Organics), benzylmercaptan [100-53-8] (99%, Sigma-Aldrich), benzyl bromide [100-39-0] (98%, Sigma-Aldrich), dichloromethane [75-09-2] (Acros Organics), $CHCl_3$ [37-297-8] (99%, Sigma-Aldrich), triethylamine [121-44-8] (99%, Acros Organics), and magnesium sulfate [7487-88-9] (97%, Acros Organics) were used as received. Tetrahydrofuran (THF) was distilled over K−Na. Styrene-d_8 [PS 07150] (99%, Chemotrade) was distilled in vacuo in the presence of hydroquinone. *N*-Isopropylacrylamide [2210-25-5] (99%, Acros Organics) was recrystallized from hexane and dried in vacuo. AIBN (Wako) was recrystallized from methanol and dried in vacuo.

2.2. Synthesis. *2.2.1. RAFT Agent Dibenzyltrithiocarbonate (DBTC).* Triethylamine (12.0 mL, 0.0805 mol) was added dropwise at ambient temperature with stirring to a mixture of benzylmercaptan (9.5 mL, 0.0805 mol), CS_2 (6 mL, 0.0805 mol), and dry $CHCl_3$ (120 mL). The solution became yellow/orange as the addition proceeded with formation of the intermediate triethylammonium butyltrithiocarbonate. After 30 min of stirring, benzyl bromide (10 mL, 0.0805 mol) was added slowly, causing the mixture to thicken with ongoing precipitation of triethylammonium bromide. The reaction mixture was stirred for 16 h and then diluted with $CHCl_3$ (80 mL) prior to washing with three portions of 100 mL of water. The organic solution was dried over $MgSO_4$, concentrated by evaporation, and passed over a short column of basic Al_2O_3. The solvent was removed by rotary evaporation to give an orange oil. Yield: 21.62 g (92.46%). Elemental analysis ($C_{15}H_{14}S_3$, M_r = 290.47): Calcd $C_{15}H_{14}S_3$. %C: 62.02; %H: 4.86; %S: 33.12. Found: %C = 62.36; %H = 4.90; %S = 32.91. ^{1}H NMR (300 MHz in $CDCl_3$, δ in ppm): δ = 4.65 (s, 4H, CH_2−aryl), 7.38−7.28 (m, 10H, aromatic H). ^{13}C NMR (75 MHz in $CDCl_3$, δ in ppm): δ = 41.48 (−S−*C*H$_2$−), 127.72 (*C*H aryl-para), 128.64 (*C*H aryl-ortho), 129.20 (*C*H aryl-meta), 134.84 (*C*-aryl), 222.63 (−S−(*C*=S)−S−).

2.2.2. Polymerization of Styrene-d_8: Synthesis of Macro-CTA1. Styrene-d_8 (10.0 g, 0.089 mol) and DBTC (0.002 mol) were purged with argon for 30 min and immersed in an oil bath at 110 °C. After 19 h, the polymerization was quenched by placing the flask into liquid nitrogen. The reaction mixture was diluted with acetone and precipitated in methanol. The precipitation was repeated twice, and the collected polymer was dried in vacuo at 50 °C for 16 h. Yield 4.0 g (40.0%) of yellow powder.

2.2.3. Polymer Chain Extension with NIPAM. In a typical procedure, NIPAM (5.10 g, 0.045 mol), the selected macro-RAFT agent (here macroCTA1; 0.2875 g, M_n = 2300 g/mol, 1.25×10^{-4} mol), and AIBN (0.0025 g, 1.56×10^{-5} mol) in THF (28 mL) were purged with argon for 15 min and immersed into an oil bath preheated to 65 °C. After 62 h, the reaction was quenched by placing the flask in liquid nitrogen. The reaction mixture was diluted with acetone and precipitated in diethyl ether (300 mL). The polymer was collected by filtration, dissolved in acetone, and dialyzed against water for 3 days. The polymer was recovered and freeze-dried. Yield: 4.08 g (80.0%) of off-white powder.

2.3. Methods. *2.3.1. Spectroscopy.* ^{1}H and ^{13}C NMR spectra were taken with an apparatus Bruker Avance 300 (300 MHz). Mass spectra were recorded by a GC/MS-system Trace DSQII (Thermo Scientific). IR spectra were taken from thin films cast on KBr pellets with a FT-IR spectrometer Bruker IFS 66/s.

2.3.2. Size Exclusion Chromatography (SEC). SEC of the polymers was run in *N*,*N*-dimethylacetamide containing 0.1% LiBr as eluent at a column temperature of 45 °C, with a setup consisting of an Agilent 1200 isocratic pump, an Agilent 1200 refractive index detector, and two GRAM columns (10 μm, 8 × 300 mm, pore sizes 100 and 1000; PSS GmbH, Mainz, Germany). The SEC setup was calibrated using low-polydispersity polystyrene standards (PSS GmbH, Mainz, Germany). Assuming an ideal RAFT mechanism[39] and that (i) the amount of initiator derived polymer chains is negligible and that (ii) the obtained yields correspond to monomer conversion, the theoretically expected number-average molar mass M_n^{theor} can be calculated in good approximation as

$$M_{theor} = (\text{conversion} \times M_{monomer} \times [M])/[CTA] + M_{CTA} \quad (1)$$

where [M] is the initial concentration of monomer, [CTA] is the concentration of RAFT agent, $M_{monomer}$ is the molar mass of

Table 1. Characteristics of the Synthesized Polymers

entry	triblock copolymer	RAFT agent	yield (%)	$M_n^{theor\,a}$	M_n (SEC)[b]	PDI[b]	M_n (UV)[c]
1	macroCTA1	DBTC	40	2290	2300	1.19	
2	P(S-d_8)$_{10}$-*b*-PNIPAM$_{390}$-*b*-P(S-d_8)$_{10}$	macroCTA1	80	35000	19700[d]	1.47	46000
3[e]	macroCTA2	DBTC	40	2290	2300	1.21	
4[f]	PS$_{11}$-*b*-PNIPAM$_{370}$-*b*-S$_{11}$	macroCTA2	86	37000	17500[d]	1.47	44000
5[g]	PS$_{11}$-*b*-PNIPAM$_{280}$-*b*-S$_{11}$	macroCTA2	89	27000	18000[d]	1.31	34000

[a] Calculated according to eq 1, assuming 100% blocking efficiency and that the molar mass of the P(S-d_8) or PS block corresponds to the one of the macroRAFT agents used. [b] In dimethylacetamide based on polystyrene standards. [c] From the absorbance at 262 nm, assuming that the molar mass of the P(S-d_8) or PS block corresponds to the one of the macroRAFT agents used. [d] Apparent values only. [e] Polymerization conditions: 0.089 mol of styrene, 2.0×10^{-3} mol of RAFT agent, 110 °C, 19 h. [f] Molar ratio NIPAM/macro RAFT agent in reaction mixture = 350/1. [g] Molar ratio NIPAM/macro RAFT agent in reaction mixture = 250/1.

the monomer, and M_{CTA} is the molar mass of the chain transfer agent.

2.3.3. Turbidimetry. Turbidity measurements were performed on a temperature-controlled turbidimeter (model TP1, E. Tepper, Germany). Solutions were prepared in demineralized H_2O at a concentration of 1 mg/mL. The transmittance of solutions was set automatically to 90% at the beginning of each measurement. The samples were heated from 20 to 60 °C and cooled down again with heating and cooling rates of 1.0 K/min, respectively. Temperatures are precise within 0.5 K.

2.3.4. Fluorescence Correlation Spectroscopy. The setup and the sample preparation have been described in ref 33. A ConfoCor 2 from Carl Zeiss Jena GmbH was used together with an Ar^+ laser (λ = 488 nm). In the solutions in demineralized H_2O, the concentration of Rh6G was kept at 50 nM, whereas the one of the polymers (PS$_{11}$-*b*-PNIPAM$_{280}$-*b*-PS$_{11}$ and PS$_{11}$-*b*-PNIPAM$_{370}$-*b*-PS$_{11}$) was varied.

2.3.5. Dynamic Light Scattering (DLS). Temperature-resolved DLS experiments on filtered solutions of the polymers at 0.1−0.2 mg/mL in demineralized H_2O were performed in polarized geometry using an ALV-5000/E correlator together with a goniometer with an index matching vat filled with toluene. The light source was a Nd:YAG laser operated at λ = 532 nm. The scattered light was detected at a scattering angle θ = 90° using the setup described previously.[33] At each temperature, measurements of duration 4−10 min were performed. After each temperature change, the waiting time was 20 min. Additional θ-dependent measurements of the solution of PS$_{11}$-*b*-PNIPAM$_{370}$-*b*-PS$_{11}$ at 0.1 mg/mL at 20 °C showed that the relaxation rate $\Gamma \propto \sin^2(\theta/2)$; i.e., the process is diffusive. The temperature-dependent average hydrodynamic radii of the micelles or the clusters, R_h, were determined using the routine REPES,[40] as detailed in ref 33, which gives distribution functions of hydrodynamic radii. At this, the Stokes−Einstein equation, $R_h = k_BT/6\pi\eta D$, was used with D being the measured diffusion coefficient and η the viscosity of the solution.

2.3.6. Small-Angle Neutron Scattering. SANS experiments were carried out using the KWS-2 small-angle scattering instrument of the JCNS outstation at the FRM II, Garching, Germany. For the experiments, a wavelength λ = 0.7 nm ($\Delta\lambda/\lambda$ = 20%) and sample-to-detector distances (SDD) of 2 and 8 m were chosen, resulting in q-ranges of 0.049−0.45 and 0.25−1.7 nm^{-1}. The detector design is based on a modified Anger technology with a ^{6}Li glass as a scintillator.[41] The solutions of P(S-d_8)$_{10}$-*b*-PNIPAM$_{390}$-*b*-P(S-d_8)$_{10}$ having concentrations of 50 and 220 mg/mL (ref 42) were mounted in standard Hellma quartz cuvettes (light path of 1 or 2 mm). The exposure times per image were between 5 and 20 min for different concentrations and detector configurations. After each temperature change, the waiting time was 15 min. The background of the cuvette was subtracted from the sample scattering, taking the transmissions into account. The intensities were corrected for dark current and background using the scattering of boron carbide. The scattering of poly(methyl methacrylate) was used for measuring the detector sensitivity and for bringing the intensities on an absolute scale. The 2D scattering images were isotropic, and hence, the intensities were azimuthally averaged. All data reduction was performed with the software qtiKWS provided by JCNS.

The scattering length densities of the polymer blocks, $\delta_{P(S\text{-}d_8)} = 6.42 \times 10^{10}$ cm^{-2} and $\delta_{PNIPAM} = 0.79 \times 10^{10}$ cm^{-2}, were calculated based on the scattering length densities of the elements and the specific volumes, v = 0.952 mL/g for PS and 0.892 mL/g for PNIPAM in water.[43] Contrast matching of the core or the shell block was performed by using either pure D_2O or a 20:80 v/v mixture of D_2O ($\delta_{D_2O} = 6.38 \times 10^{10}$ cm^{-2}) and H_2O ($\delta_{H_2O} = -0.56 \times 10^{10}$ cm^{-2}) as a solvent.

The SANS curves were analyzed using the software Scatter 2.0.[44] This software was able to fit the combination of the form factor of polydisperse spherical core−shell particles, $P(q)$ (q is the magnitude of the scattering vector), as well as a Percus−Yevick structure factor, $S(q)$, describing their liquidlike correlation, to the curves. Above the LCST, additional forward scattering at $q < 0.15$ nm^{-1} was present. Prior to using Scatter 2.0, the forward scattering was modeled by an algebraic decay $I(q) \propto K/q^\kappa$. This contribution was subtracted from the SANS curve, and the remainder was used with Scatter 2.0. Finally, both contributions were summed up to give the fitted curve $I(q) = I_0S(q)P(q) + K/q^\kappa$. The incoherent background due to the solvent and the polymer was treated as a fitting parameter and was found to lie in a reasonable range.

2.3.7. Neutron Spin-Echo Spectroscopy (NSE). Experiments were carried out at J-NSE at FRM-II.[45,46] The Fourier times ranged from 0.1 to 60 ns. The measurement of one curve up to Fourier times of 60 ns took ~11 h. The sample temperature was controlled by circulating thermostated water with a precision of ±0.1 K. Grafoil or graphite powder was used to measure the resolution function of the spectrometers. The detector was a multiwire area detector. The detector was placed at average q-values of 0.8, 1.1, 1.5, and 1.8 nm^{-1}. Temperature scans were carried out at q = 1.5 nm^{-1}. Samples were prepared by dissolving P(S-d_8)$_{10}$-*b*-PNIPAM$_{390}$-*b*-P(S-d_8)$_{10}$ in D_2O at concentrations of 50, 200, and 300 mg/mL. The samples were mounted in Hellma Quartz cells of size 30 mm × 30 mm with a sample thickness of 4 mm for the lowest concentration (50 mg/mL) and 2 mm for 200 and 300 mg/mL.

3. Results

3.1. Synthesis and Molecular Characterization. The synthesis of the nondeuterated polymers (Table 1) by the RAFT method[39] using the well-established bifunctional trithiocarbonate DBTC as chain transfer agent followed the procedure described in ref 34. In this work, we describe the analogous synthesis of the triblock copolymer P(S-d_8)-*b*-PNIPAM-*b*-P(S-d_8) with fully deuterated PS blocks (Scheme 1). In the first step, styrene-d_8 is thermally polymerized in the presence of DBTC. The formed polystyrene-d_8 is engaged as bifunctional macroRAFT agent macroCTA1 in the subsequent chain extension polymerization of NIPAM initiated by AIBN to produce the symmetrical triblock copolymer P(S-d_8)-*b*-PNIPAM-*b*-P(S-d_8).

The bifunctional RAFT agent DBTC was used to prepare the triblock copolymer. The initial thermal polymerization

Scheme 1. Synthesis of Triblock Copolymer P(S-d_8)-*b*-PNIPAM-*b*-P(S-d_8) via Successive RAFT Polymerizations of Styrene-d_8, Using DBTC and NIPAM

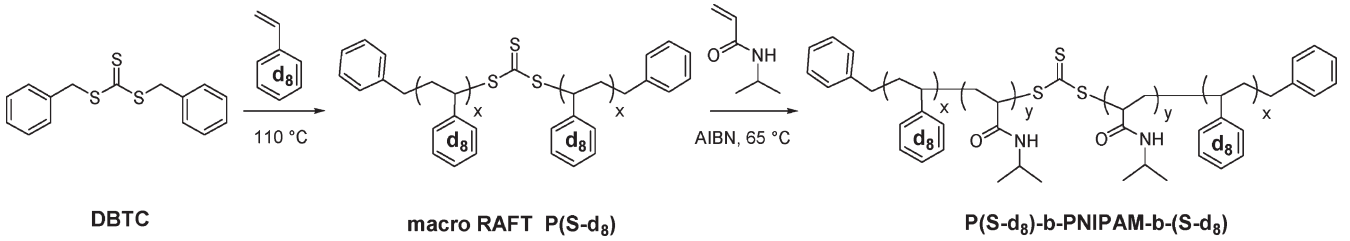

of styrene-d_8 in the presence of the DBTC (the ratio of monomer to RAFT agent was set $[M]_0/[RAFT]_0 = 45$) was conducted to moderate conversions only, in order to guarantee a high degree of end-group functionality of the polymer formed,[47,48] and thus to produce a highly efficient macro RAFT agent with a well-defined molar mass (see Figure 1a).

While the FT-IR spectrum shows the typical features of polystyrene-d_8, such as bands at 2270 cm^{-1} (C−D aryl stretching), 2195 cm^{-1} (C−D chain asymmetrical stretching), 2102 cm^{-1} (C−D chain symmetrical stretching), 840 cm^{-1} (C−D aryl out-of-plane), and 821 cm^{-1} (C−D aryl out-of-plane),[49] the ^{1}H NMR spectrum of macroCTA1 exhibits mainly the signals of the initiating benzyl groups at both chain ends (Figure 1b) due to the high degree of deuteration of the styrene-d_8 (99%). The analysis of macroCTA1 by SEC shows a monomodal, relatively narrow molar mass distribution (Figure 1a), with a number-average molar mass M_n of 2300 (corresponding to an average degree of polymerization of 20.5) and a polydispersity index PDI of 1.19. Assuming an ideal RAFT mechanism, the theoretically expected number-average molar mass M_n^{theor} is calculated as 2290 using eq 1. Additionally, the average degree of polymerization can be calculated from the sulfur content of the elemental analysis, assuming that all polymers contain exactly the fragments of one molecule of DBTC, to yield a number-average degree of polymerization of 22. The good agreement between these values demonstrates the good control over the molar mass of macroCTA1 as well as its high content of RAFT active end groups, as needed for the successful synthesis of the triblock copolymers.

Subsequently, the polystyrene-d_8 was employed as bifunctional macroRAFT agent for chain extension with NIPAM in order to prepare amphiphilic triblock copolymers of the BAB type. The successful chain extension of the macroCTA1 by NIPAM is qualitatively shown by ^{1}H NMR. The spectrum exhibited in Figure 1c with strong signals at 4 ppm (characteristic for the CON−CH⟨ methine proton) and at 6.4−7.6 ppm (characteristic for the CONH⟨ amide proton) evidences the incorporation of NIPAM in large quantities. The benzyl end groups which were visible in the spectrum of macroCTA1 are camouflaged by the much larger signal of the amide protons. The successful chain extension is further corroborated by SEC. The polymer obtained shows a monomodal molar mass distribution with a PDI value of 1.47 and an apparent number-average molar mass of $M_n^{app} = 19\,700$ based on calibration with polystyrene (Figure 1a).

It is difficult to determine the absolute mass of the triblock copolymer precisely, as several problems are superposed. This comprises the amphiphilic character of the block copolymer with a strong tendency to aggregate in solution and the unfavorable combination of a very large block, namely of PNIPAM, that is hygroscopic with a very short one, namely of polystyrene-d_8, that is virtually invisible in the ^{1}H NMR.

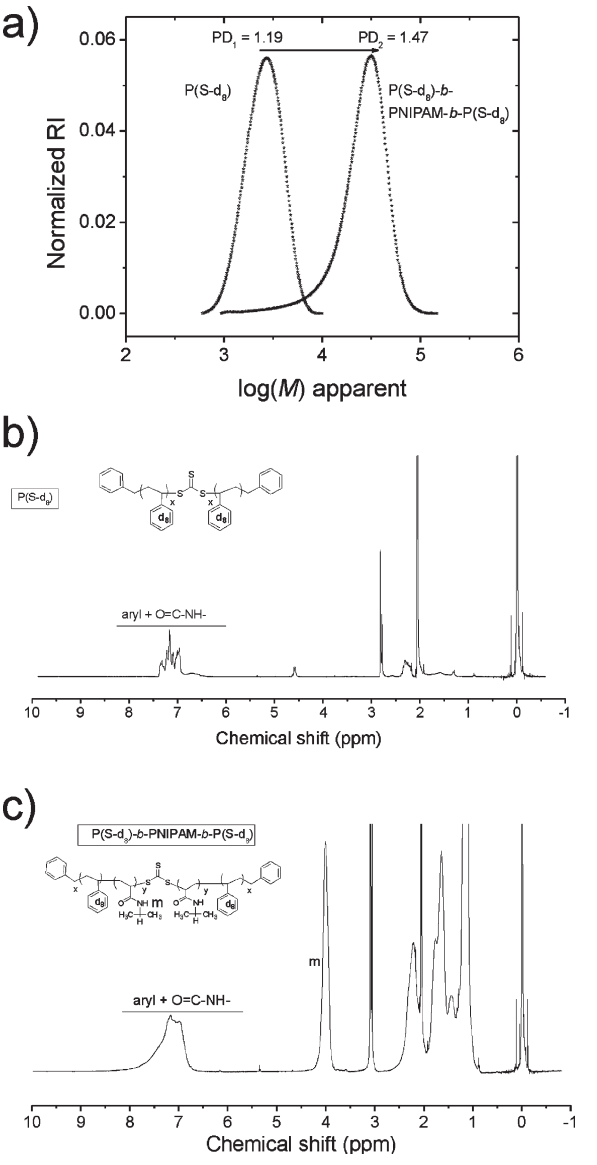

Figure 1. Molecular characterization of triblock copolymer P(S-d_8)$_{10}$-*b*-PNIPAM$_{390}$-*b*-P(S-d_8)$_{10}$ and its precursor macroRAFT1. (a) SEC elugrams of triblock copolymer (right curve) and of macroRAFT1 (left curve). (b) ^{1}H NMR spectrum of macroRAFT1. (c) ^{1}H NMR spectrum of triblock copolymer (both spectra in acetone-d_6).

When assuming that the molar mass of the polystyrene-d_8 block of 2300 is preserved in the block copolymer, the C/N ratio from elemental analysis enables in principle to calculate the absolute molar mass. Still, due to the small size of the polystyrene block, this analysis provides only an approximate value. The thus—formally—calculated value of 55 700 ± 28 000 for the block copolymer implies a number-average

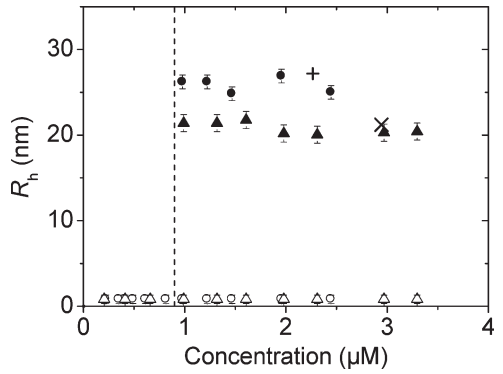

Figure 2. Results from FCS on aqueous solutions of PS_{11}-*b*-$PNIPAM_{280}$-*b*-PS_{11} (triangles) and PS_{11}-*b*-$PNIPAM_{370}$-*b*-PS_{11} (circles) with Rh6G as tracers as a function of the copolymer concentration. The concentration of Rh6G was kept constant at 50 nM. The temperature was 27 °C. Open symbols: free Rh6G; closed symbols: micelles carrying Rh6G. The dashed vertical line marks the resulting critical micelle concentration at 0.9 μM. Results from DLS at 27 °C on PS_{11}-*b*-$PNIPAM_{280}$-*b*-S_{11} (cross) and PS_{11}-*b*-$PNIPAM_{370}$-*b*-S_{11} (plus).

degree of polymerization of 500 ± 250 of the PNIPAM block. A more reliable value can be derived from the absorbance of the styrene moieties in the UV spectrum.[50] On the basis of the extinction coefficient of polystyrene at 262 nm in CH_2Cl_2 of 222.5 L mol^{-1} cm^{-1}, we calculate a molar mass of 46 300 ± 13 000 for the triblock copolymer, assuming again that the molar mass of the polystyrene-d_8 block of 2300 is preserved in the block copolymer. This means a number-average degree of polymerization of 390 of the PNIPAM block.

3.2. Micelle Formation. The critical micelle concentration (cmc) of amphiphilic block copolymers is usually very low and cannot be determined by scattering methods, but by fluorescence correlation spectroscopy (FCS) which allows to access sufficiently low polymer concentrations.[33,51−53] To determine the cmc of PS-*b*-PNIPAM-*b*-PS as a function of N_{PNIPAM} below the LCST, poorly water-soluble fluorescent dyes, such as Rh6G, at very low concentration (50 nM) served as tracers in dilute solutions of PS_{11}-*b*-$PNIPAM_{280}$-*b*-PS_{11} and PS_{11}-*b*-$PNIPAM_{370}$-*b*-PS_{11}, which were directly dissolved in H_2O. Below the cmc, the dye molecules stay molecularly dissolved in H_2O, and only the diffusion of free dye is expected. Above the cmc, in contrast, a fraction of the dye molecules attach to the micelles, and an additional slow diffusional decay is expected in the FCS correlation curve. At low concentrations, the correlation curves can be fitted with a single decay leading to R_h = 0.8 nm, the value expected for free Rh6G.[52] The hydrodynamic radii deduced from the decay times are shown as a function of polymer concentration in Figure 2. Above a polymer concentration of 0.9 μM, a second, slower decay is present in the correlation curves with hydrodynamic radii of 20.8 ± 0.7 nm for PS_{11}-*b*-$PNIPAM_{280}$-*b*-PS_{11} and 25.8 ± 0.9 nm for PS_{11}-*b*-$PNIPAM_{370}$-*b*-PS_{11}. Micelles are thus present in the solution, and a fraction of the Rh6G molecules attaches to them. In another amphiphilic block copolymer system, we have shown that the cmc determined by using Rh6G is the same as when using the identical, fluorescence-labeled block copolymer as a tracer.[53] We note that already below the polymer concentration of 0.9 μM micelles might be present, but too few to solubilize Rh6G. The cmc is thus at 0.9 μM or lower. The R_h value of the micelles determined using DLS at concentrations of 0.1 mg/mL coincides with the values from FCS, confirming the assignment of the slow FCS decay to micelles.

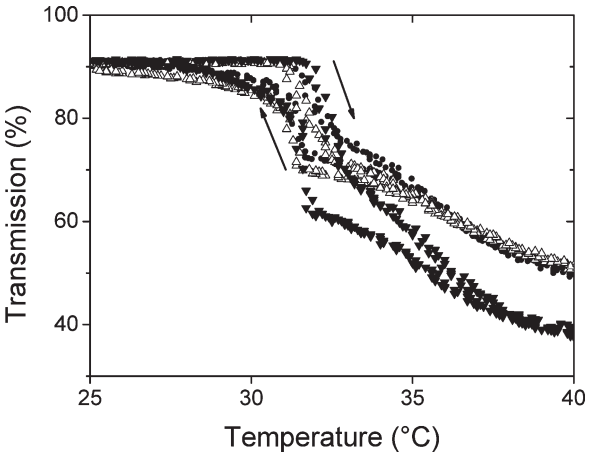

Figure 3. Temperature-dependent light transmission of 1 mg/mL aqueous solutions of PS_{11}-*b*-$PNIPAM_{280}$-*b*-PS_{11} (open triangles up), PS_{11}-*b*-$PNIPAM_{370}$-*b*-PS_{11} (filled circles), and $P(S\text{-}d_8)_{10}$-*b*-$PNIPAM_{390}$-*b*-$P(S\text{-}d_8)_{10}$ (filled triangles down). The arrows denote heating and cooling.

We conclude that the cmc of P(S-*b*-NIPAM-*b*-PS) is located at 0.03−0.04 mg/mL for both polymers and that the micellar hydrodynamic radius increases with PNIPAM molar mass, as expected.[31,33,52,54,55] The behavior is very similar to the one observed with the previously studied PS_{48}-*b*-$PNIPAM_{159}$ diblock copolymer in dilute aqueous solution.[33]

3.3. Collapse Transition. Turbidity measurements were carried out to determine the cloud point as a function of N_{PNIPAM}. To ensure that the majority of the polymers is arranged in micelles, a concentration well above the cmc was chosen (1 mg/mL) for all solutions. At low temperatures, the solutions are clear and suddenly become turbid at 31−32 °C. This is measured in the light transmission curve which decreases steeply in this temperature range (Figure 3). Thus, the cloud point has been reached, and large clusters are formed by the collapsed, hydrophobic micelles which scatter light strongly. Above ~33 °C, all curves show a shoulder and reach a plateau at 40−50% of the initial value at ~40 °C. This shoulder may be due to the mechanism of cluster growth. Upon cooling, hysteresis is observed, but nevertheless the process is fully reversible. The resulting cloud point temperatures increase with N_{PNIPAM} from 31.1 to 31.7 °C. The shoulder and the hysteresis have previously been observed with a micellar solution of PS-*b*-PNIPAM diblock copolymers where bridging is absent.[33] We thus ascribe this behavior to the hydrophobic interactions between the collapsed micelles.

To characterize the structural changes in micellar solutions at the LCST in more detail, we have carried out temperature-resolved DLS experiments on PS_{11}-*b*-$PNIPAM_{370}$-*b*-PS_{11} and $P(S\text{-}d_8)_{10}$-*b*-$PNIPAM_{390}$-*b*-$P(S\text{-}d_8)_{10}$ in H_2O. To minimize the interaction between micelles, concentrations of 0.1−0.2 mg/mL were chosen, which are only slightly above the cmc. The hydrodynamic radii obtained for PS_{11}-*b*-$PNIPAM_{370}$-*b*-PS_{11} at 0.1 mg/mL show a shallow decay from 27 nm at 25 °C to 23 nm at 30 °C (Figure 4). At the cloud point determined from turbidimetry (31.4 °C), the hydrodynamic radius does not decrease, as expected for single collapsing micelles, but increases within 1.6 K to 29 nm. We attribute this length scale to small clusters consisting of several collapsed micelles. This behavior is very different from what we observed with PS-*b*-PNIPAM diblock copolymers, where single collapsed micelles could clearly be detected above the LCST.[33] We conclude that

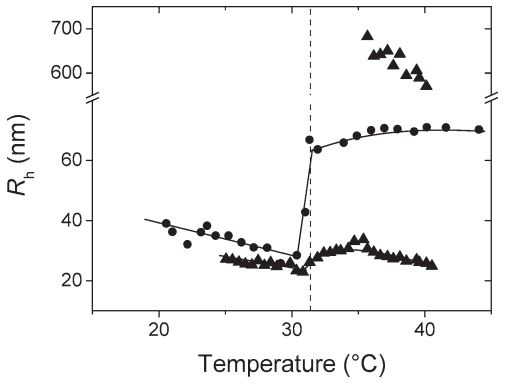

Figure 4. Hydrodynamic radii, R_h of the micelles in H_2O from DLS. Triangles up: PS_{11}-*b*-$PNIPAM_{370}$-*b*-PS_{11} at 0.1 mg/mL; circles: P(S-d_8)$_{10}$-*b*-$PNIPAM_{390}$-*b*-P(S-d_8)$_{10}$ at 0.2 mg/mL, both measured at $\theta = 90°$. The full lines are guides to the eye. The dashed line marks the collapse transition temperature from turbidimetry (31.4 °C, Figure 3).

already after dissolution in H_2O at room temperature the micelles formed by PS_{11}-*b*-$PNIPAM_{370}$-*b*-PS_{11} are bridged, even at this low concentration. Above 35 °C, additional large objects (550−700 nm) are observed, which are presumably very large clusters formed by collapsed micelles and the existing small clusters.

Similar characteristics are observed for the triblock copolymer P(S-d_8)$_{10}$-*b*-$PNIPAM_{390}$-*b*-P(S-d_8)$_{10}$ at 0.2 mg/mL (Figure 4). With this polymer, the clusters formed above the collapse temperature are larger than in PS_{11}-*b*-$PNIPAM_{370}$-*b*-PS_{11}, presumably due to the slightly higher concentration. In contrast, no large clusters are observed, even at high temperatures.

The hydrodynamic radii of the swollen micelles formed by the triblock copolymers below the collapse temperature, e.g., 27.2 nm for PS_{11}-*b*-$PNIPAM_{370}$-*b*-PS_{11} and 34.7 nm for P(S-d_8)$_{10}$-*b*-$PNIPAM_{390}$-*b*-P(S-d_8)$_{10}$ at 25 °C, are significantly smaller than the value of the PS_{48}-*b*-$PNIPAM_{159}$ diblock copolymer studied by us previously (41 nm at 25 °C).[33] The geometric effect of the polymer architecture—starlike vs flowerlike micelles—is not expected to have a significant influence on the shell thickness, since the molar mass of the PNIPAM block in the diblock copolymer is roughly one-half of the ones of the triblock copolymers studied here. We attribute the discrepancy to the difference in core size resulting from the difference in N_{PS} and, therefore, in aggregation number, N_{agg}. Using the relations for the radius of gyration of the PS block in the melt, $R_g \propto N^{1/2}$, together with $N_{agg} \propto R_g^3$, we estimate N_{agg} of the triblock copolymers to be a factor of 10 lower than the one of the diblock copolymer, which is at the origin of the size difference.

The decrease of R_h of the swollen micelles with increasing temperature toward the collapse temperature has previously been observed with diblock and triblock copolymers from PS and PNIPAM.[29,31,33] Since the core size remains constant (see section on SANS below), the decrease must be due to a relaxation of the PNIPAM shell blocks toward a more coiled conformation.

The clustering just above the collapse transition is readily explained by the increased hydrophobicity of the formerly hydrophilic PNIPAM block. Clusters of similar size (R_h = 70−90 nm) have been observed with the above-mentioned PS-*b*-PNIPAM diblock copolymer as well.[33] However, in the diblock copolymer, they were only observed above 40 °C, whereas in the triblock copolymers, they form right above the collapse transition, and single, collapsed micelles cannot be detected. We conclude that the ability of the triblock copolymers to bridge two micellar cores[56−58] results in more pronounced cluster formation than in the diblock copolymer where the clusters are only connected by hydrophobic interactions. Only in very dilute solutions ($< 10^{-3}$ mg/mL) of PS-*b*-PNIPAM-*b*-PS triblock copolymers, the collapse of single micelles could be observed.[31]

3.3. Collapse Transition in Concentrated Solutions. The core−shell structure of the micelles, the collapse of the micellar shell, and the correlation of the micelles as a function of temperature were investigated by SANS. Two contrasts were exploited to study the polymer P(S-d_8)$_{10}$-*b*-$PNIPAM_{390}$-*b*-P(S-d_8)$_{10}$: In D_2O, the P(S-d_8) core was contrast-matched, and we were able to highlight the thermoresponsive PNIPAM shell. Using a 20:80 v/v mixture of D_2O/H_2O, the PNIPAM shell was matched and the P(S-d_8) core was highlighted, however, at the expense of a higher scattering background. It must be kept in mind, though, that H/D exchange can occur in the amide group of PNIPAM during the equilibration time before the measurements (a few days).[59] At a relatively low concentration (50 mg/mL), we could characterize the micelles in the absence of strong correlation. Solutions with a higher concentration (220 mg/mL) enabled us to investigate the correlations between the micelles as well as their changes at the collapse transition.

The SANS curves at 50 mg/mL in D_2O/H_2O and in D_2O are shown in Figure 5. Below the collapse temperature, the curves in D_2O/H_2O are expected to show the scattering from weakly interacting micellar P(S-d_8) cores, since the PNIPAM shell is contrast-matched by the solvent (Figure 5c). The curves measured at the same concentration in D_2O (Figure 5a) are expected to be entirely due to the scattering of the PNIPAM blocks. They show qualitatively the same behavior: A weak correlation peak is observed at 0.16 nm^{-1}, corresponding to an approximate intermicellar distance of 40 nm. At higher *q*-values, shoulders due to the micellar form factor are present. As the collapse temperature is approached, the correlation peak becomes less pronounced. Above the collapse temperature, the curve shapes change drastically (Figure 5b,d). The curves right at the collapse temperature show a continuous decay, indicating fluctuations on a wide range of length scales. At higher temperatures, again a correlation peak is observed at a much higher *q*-value ($\sim$0.44 nm^{-1}) than below the collapse temperature, which indicates that the intermicellar distance decreases by a factor of $\sim$2.8 upon collapse. Moreover, the form factor is slightly altered. However, the most prominent feature is the strongly increased forward scattering which is due to the formation of large clusters of micelles.

Below the collapse temperature, both sets of curves can be modeled successfully with a form factor for spherical core−shell micelles together with a Percus−Yevick structure factor. Fitting of a model for homogeneous spheres representing the P(S-d_8) core to the curves measured in D_2O/H_2O was not successful, and it was necessary to include scattering from the shell. Reasons may be a slight bias in the contrast matching or the H/D exchange between the amide group in PNIPAM and D_2O prior to the measurement. For both sets of data, the core radius amounts to $R_{core} = 3.0 \pm 0.5$ nm in the entire temperature range (Figure 6a). Using the mass density of bulk PS of 1.05 g/cm^3 and the degree of polymerization of both PS blocks (2300 g/mol), this size corresponds to an aggregation number $N_{agg} = 31 \pm 15$, which is in the usual range. The micellar radius, $R_{micelle}$, as determined in D_2O, is 17 ± 1 nm below the collapse temperature and decreases slightly as the collapse temperature is approached, which points to an incipient collapse already below the LCST. In the curves from D_2O/H_2O, the

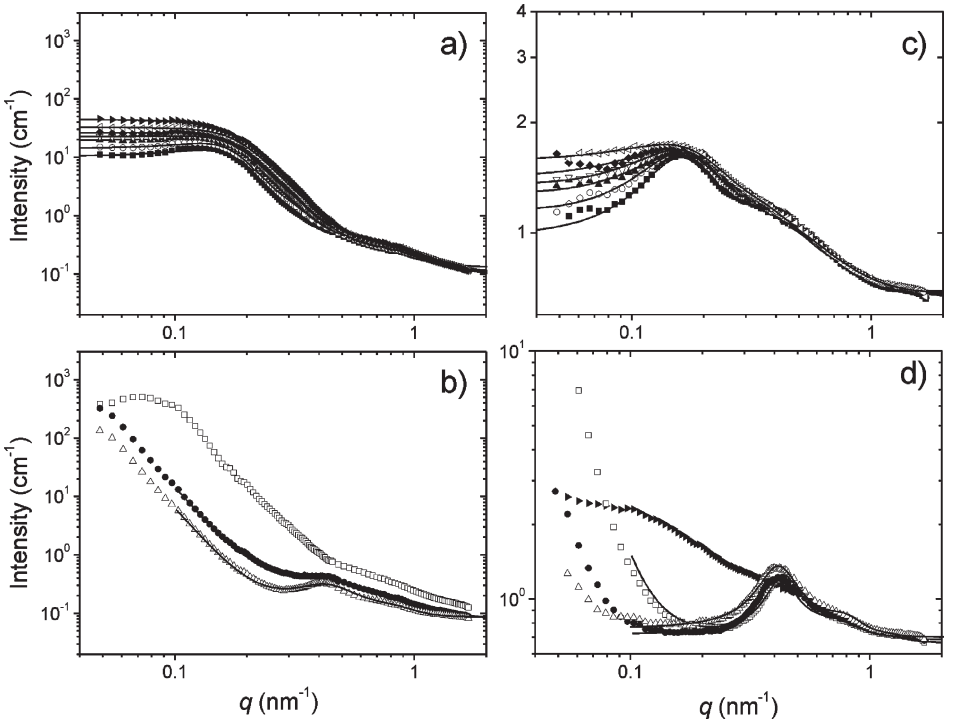

Figure 5. SANS curves of P(S-d_8)$_{10}$-*b*-PNIPAM$_{390}$-*b*-P(S-d_8)$_{10}$ at 50 mg/mL in (a, b) D_2O and (c, d) in D_2O/H_2O. Experimental curves: filled squares, 20 °C; open circles, 25 °C; filled triangles up, 28 °C; open triangles down, 29 °C; filled diamonds, 30 °C; open triangles left, 31 °C; filled triangles right, 32 °C; open squares, 33 °C; filled circles, 35 °C; open triangles up, 40 °C. The lines are fits; see text. The curves at 35 and 40 °C in (b) have lower overall intensities which we attribute to sedimentation.

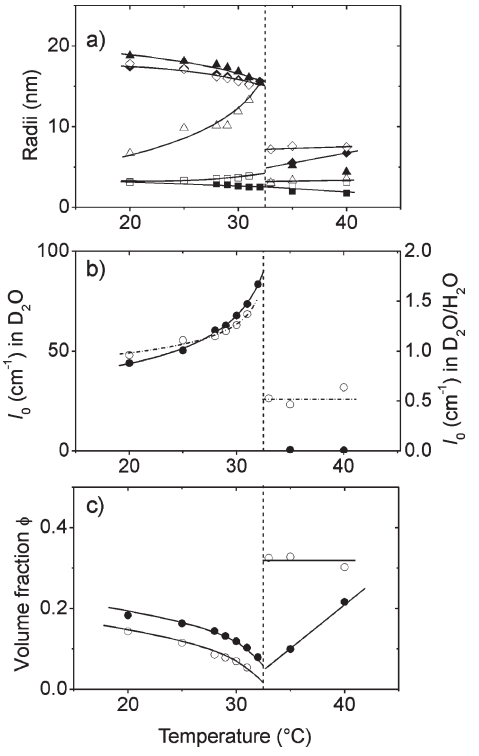

Figure 6. SANS results from the fits in Figure 5 (50 mg/mL). Filled symbols: in D_2O; open symbols: in D_2O/H_2O. The dashed line marks the collapse transition. (a) Radii: squares, core radius; triangles up, micellar radius; diamonds, hard-sphere radius. (b) Forward intensity I_0. The lines below the LCST are fits; see text. (c) Volume fraction of correlated micelles, ϕ. Full lines are guides to the eye.

apparent $R_{micelle}$ value increases from 6.7 nm at 20 °C to 13.3 nm at 31 °C. We attribute this unexpected increase to pretransitional changes of the shell structure. An initial concentration gradient in the micellar shell with more dense packing near the core may be equilibrated at higher temperature.

The presence of a structure factor indicates a certain correlation already at this relatively low concentration, which may be due to both the steric interaction and a certain degree of bridging between the micelles. Such a correlation was not observed with the PS-*b*-PNIPAM diblock copolymers studied previously at a concentration of 30 mg/mL;[33] i.e., both the higher concentration and the bridging may be at the origin of the correlation. Below the collapse temperature, the hard-sphere radius, which corresponds to half the distance between micelles, is $R_{HS} = 16.3 \pm 1.0$ nm; i.e., within the errors it is similar to $R_{micelle}$. Thus, the micellar shells of the correlated micelles touch each other, which is due to the limited stretching of the bridging PNIPAM blocks.

The forward intensity, I_0, reflects the osmotic compressibility of the micellar solution.[60] In both solutions, I_0 increases as the collapse temperature is approached (Figure 6b); i.e., the compressibility increases because of strong fluctuations of the micellar distance. In PNIPAM homopolymers, the spinodal temperature, T_s, has been determined using the mean-field relation $I_0 \propto (T - T_s)^{-\eta}$.[61] In D_2O, where the PNIPAM shell is seen, we find $\eta = -0.39 \pm 0.04$ and $T_s = 34.9 \pm 0.6$ °C. T_s is higher than the collapse temperature of 32.5 ± 0.5 °C; i.e., the collapse of the tethered blocks preempts the expected spinodal decomposition. The exponent η differs strongly from the value of -0.8 found for PNIPAM homopolymers which we attribute to the tethering. The volume fraction of correlated micelles, ϕ, as determined from the Percus−Yevick structure factor (Figure 6c) decreases in both solutions, as the collapse transition is approached, which corroborates the notion of strong fluctuations.

Above the collapse temperature, $R_{micelle}$ drops to 4.8 ± 0.6 nm in D_2O; i.e., the partially deuterated, collapsed PNIPAM

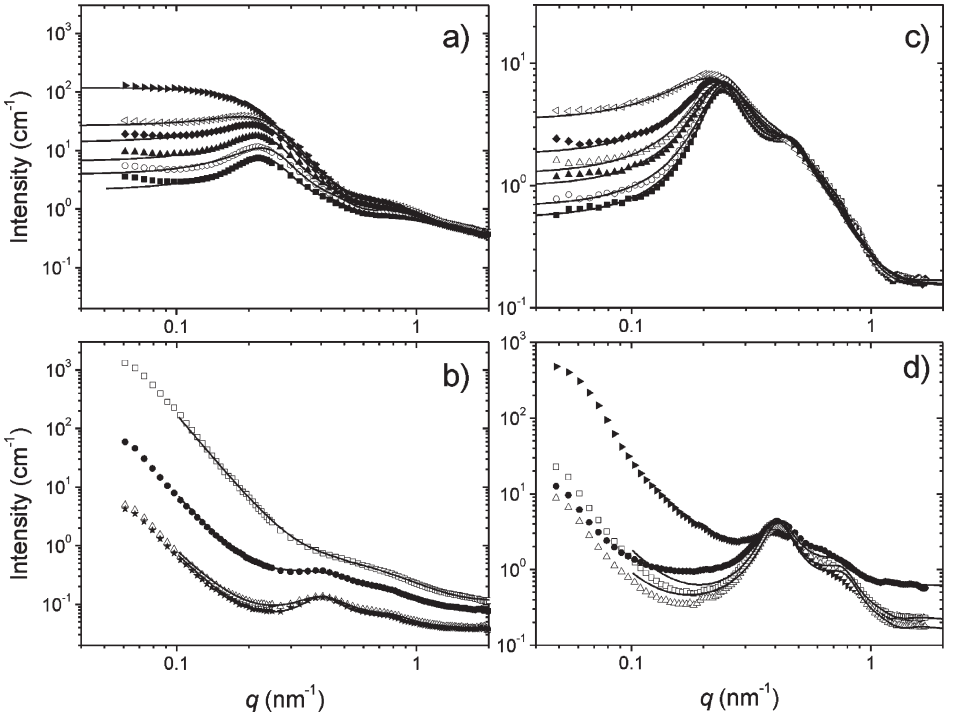

Figure 7. SANS curves of P(S-d_8)$_{10}$-*b*-PNIPAM$_{390}$-*b*-P(S-d_8)$_{10}$ at 220 mg/mL in (a, b) D_2O and (c, d) in D_2O/H_2O.[42] Same symbols as in Figure 5.

shell is much thinner (~1.5 nm) than below, whereas the core radius is unaltered (Figure 6a). In contrast to telechelic PNIPAM,[26] the core−shell structure is preserved. R_{HS} is 6.1 ± 0.9 nm, thus slightly larger than $R_{micelle}$; i.e., the micelles form a close-packed structure in the collapsed state. I_0 and ϕ are kinetically determined above the collapse temperature and are therefore not discussed further.

Heating the solutions above the collapse temperature leads to a drastic increase in forward scattering together with a shift of the correlation peak to a significantly higher q-value, 0.44 nm^{-1}; i.e., the distance between the micelles decreases, and clusters are formed due to the collapse of the shell. The forward scattering follows approximately a Porod law; i.e., the clusters are compact objects.

Solutions of higher concentration (220 mg/mL) show the same overall behavior (Figure 7) with higher scattering intensities, as expected. The structure factor is more pronounced than at lower concentration; i.e., a higher fraction of micelles are correlated. A striking difference is that, in D_2O solution, $R_{micelle}$ below the collapse temperature (11.7 ± 1.3 nm) is significantly lower than at 50 mg/mL (17 ± 1 nm) which may be attributed to the higher degree of bridging of the micelles at the higher concentration, hampering the full swelling of PNIPAM (Figure 8a). $R_{micelle}$ increases slightly toward the collapse transition. R_{HS} stays constant over the entire temperature range below the collapse temperature (12.9 ± 0.7 nm). Again, the value is smaller than at 50 mg/mL.

The temperature dependence of I_0 in D_2O shows a power law behavior as well with a slight deviation near the collapse transition (Figure 8b). The value $\eta = -0.76 \pm 1.60$ is close to the value found for PNIPAM homopolymers (albeit the error is large), and T_s = 32.0 ± 0.05 °C is close to the collapse temperature. This better agreement with PNIPAM homopolymer solutions is presumably due to the higher concentration as compared to the value from 50 mg/mL and the consequently more homogeneous PNIPAM matrix. As expected, the volume fraction of correlated micelles

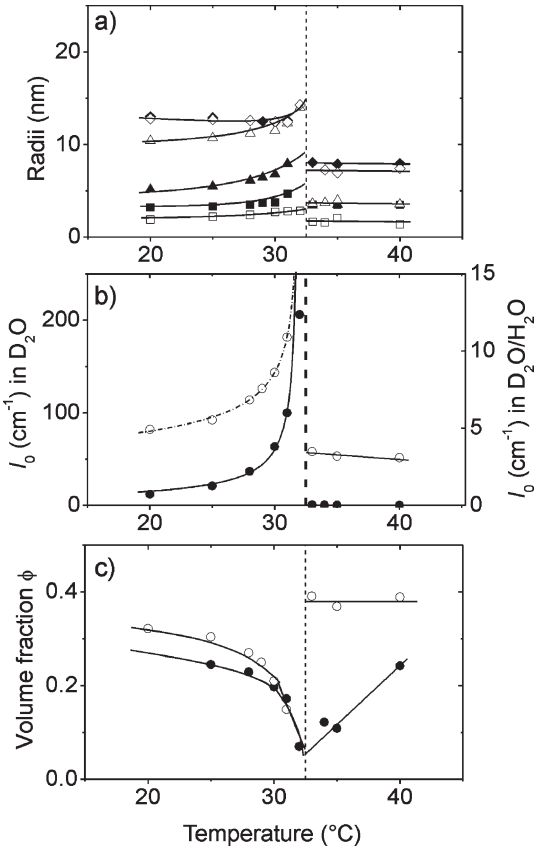

Figure 8. SANS results from 220 mg/mL (Figure 7). Same symbols as in Figure 6.

(Figure 8c) is higher than at 50 mg/mL and shows similar temperature behavior.

Above the collapse temperature, all radii are very similar to those at 50 mg/mL. In D_2O, $R_{micelle}$ decreases to 4.8 ± 0.6 nm. The shell thickness thus decreases from 9.5 to 1.5 nm,

a shrinkage of 84%, which is similar to the value obtained with the lower concentration. R_{HS} decreases to 7.2 ± 0.2 nm (in D_2O) or 8.0 ± 0.1 nm (in D_2O/H_2O), also similar to the values at lower concentration. The shrinkage of the micellar distance thus amounts to 44% in D_2O and to 37% in D_2O/H_2O.

From the above results, we conclude that a core−shell model with a homogeneous shell fits the SANS curves sufficiently well. We note here that the micelles (i.e., the building blocks) are much smaller than the microgels[16−19] and the cross-linked core−shell particles[20−23] presented in the literature. As a consequence, they are expected to react faster to temperature changes than microgels and cross-linked core−shell particles, which is of interest for applications. The PS-*b*-PNIPAM-*b*-PS triblock copolymers discussed in the literature[8,31,37] have throughout higher degrees of polymerization of the PS block ($N_{PS} \cong 35-200$); i.e., the cores are significantly larger than in our study, and the volume fractions of PNIPAM are lower. Thus, our system is able to swell more strongly.

3.4. Segmental Dynamics. The segmental dynamics of concentrated solutions of P(S-d_8)$_{10}$-*b*-PNIPAM$_{390}$-*b*-P(S-d_8)$_{10}$ triblock copolymers in D_2O have been investigated using neutron spin-echo spectroscopy (NSE).[62] Because the *q*-values chosen are relatively large, the experiment is sensitive to the local dynamics in the PNIPAM shell. The P(S-d_8) cores do not contribute to the intermediate scattering function, $S(q,t)$, because P(S-d_8) is contrast-matched by the solvent, D_2O. The signal obtained is thus entirely due to PNIPAM segmental dynamics.

In the literature, two cases have been distinguished for the segmental dynamics of the shell block: In loosely packed shells of "hairy" micelles (i.e., long shell blocks), the single-chain Zimm dynamics dominates.[63] In contrast, in densely packed shells of "crew-cut" micelles from diblock copolymers (i.e., short shell blocks), the breathing mode was observed to dominate, i.e., the cooperative motion of polymer chains in the solvent.[64,65] This breathing mode was also observed in micelles formed by triblock copolymers,[66] where the grafting density of the shell blocks at the core surface is high. These two processes are distinguished by the *q*-behavior of the relaxation rate Γ of the process: $\Gamma \propto q^2$ and $\Gamma \propto q^3$ have been predicted for the breathing mode and the single-chain dynamics, respectively. In addition to the segmental dynamics, the diffusion of micelles has been found to contribute to the intermediate structure factor at high Fourier times.[64,65]

We have investigated three concentrations between 50 and 300 mg/mL. As evident from the SANS measurements, the overlap between the PNIPAM shells becomes more and more important as concentration is increased. The intermediate scattering functions for the three concentrations are shown in Figure 9. At temperatures up to 31 °C, the curves show two decays: a dominating, fast one decaying below 10 ns and a slow one above. We attribute the fast decay to the PNIPAM shell dynamics. The latter, slow decay has low amplitude and is arrested above the collapse temperature. We attribute it to the diffusion of micelles which is slowed down above the collapse temperature due to the cluster formation of the collapsed micelles.

We have analyzed the curves in two ways: It was assumed that (i) the segmental dynamics and the micellar diffusion are completely decoupled from each other or (ii) that they are coupled.[64] The first case was described by the following equation:

$$\frac{S(q,t)}{S(q,0)} = c[A_{fast}\exp(-\Gamma_{internal}t) + (1-A_{fast})\exp(-\Gamma_{micelle}t)] \quad (2)$$

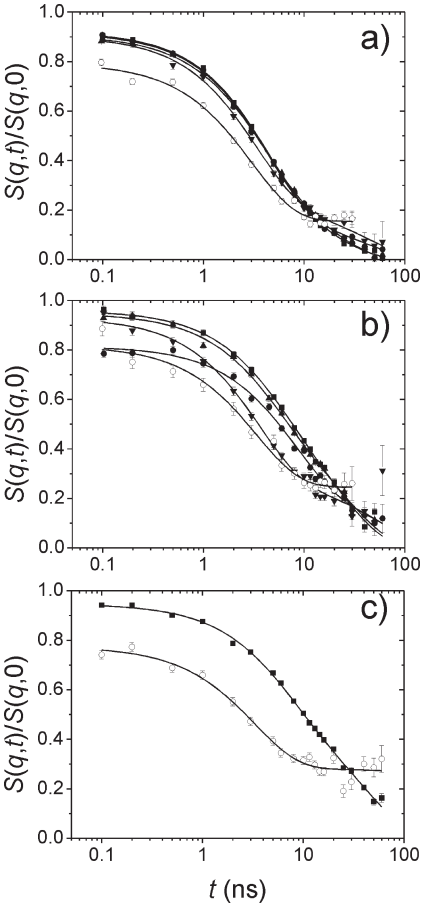

Figure 9. Representative intermediate scattering functions from NSE on P(S-d_8)$_{10}$-*b*-PNIPAM$_{390}$-*b*-P(S-d_8)$_{10}$ in D_2O: (a) 50, (b) 200, and (c) 300 mg/mL. Filled squares, 24.4 °C; filled circles, 30.5 °C; filled triangles up, 31.0 °C; filled triangles down, 32.2 °C; open circles, 33.9 °C. The solid lines are fits of eq 3 with $\Gamma_{micelle}$ as a free fitting parameter.

with A_{fast} the amplitude of the fast decay due to the internal dynamics and $\Gamma_{internal} = D_{internal}q^2$ and $\Gamma_{micelle} = D_{micelle}q^2$ the relaxation rates of the fast and the slow decay, respectively. $D_{internal}$ is the diffusion coefficient of the segmental dynamics, and $D_{micelle}$ is the diffusion coefficient of the micelles. *t* is the Fourier time. *c* denotes a factor accounting for $S(q,t)/S(q,0)$ values lower than unity. The coupled case is modeled by

$$\frac{S(q,t)}{S(q,0)} = c[(1-A_{fast}) + A_{fast}\exp(-\Gamma_{internal}t)]\exp(-\Gamma_{micelle}t) \quad (3)$$

Since we attribute the slow decay to micelle diffusion, we measured $D_{micelle}$ at the lowest concentration (50 mg/mL) at temperatures below the LCST using DLS. This value was used afterward as a fixed input parameter in eqs 2 and 3, which reduces the number of adjustable parameters. For instance, we obtained from DLS at 24.4 °C $D_{micelle} = 9.4 \times 10^{-10}$ m^2/s, which corresponds to a micellar hydrodynamic radius of 21.0 nm. This value is consistent with the micellar radius of 17 nm determined using SANS (see above). As expected, R_h is larger than the geometric radius because the swollen micelle drags along a shell of water when diffusing. Using this value of $D_{micelle}$ as a fixed parameter in the fit of eqs 2 and 3 (Figure 10), it is seen that the fitted curve lies in both cases above the experimentally determined intermediate scattering function for $t = 20-60$ ns. However, the fast decay

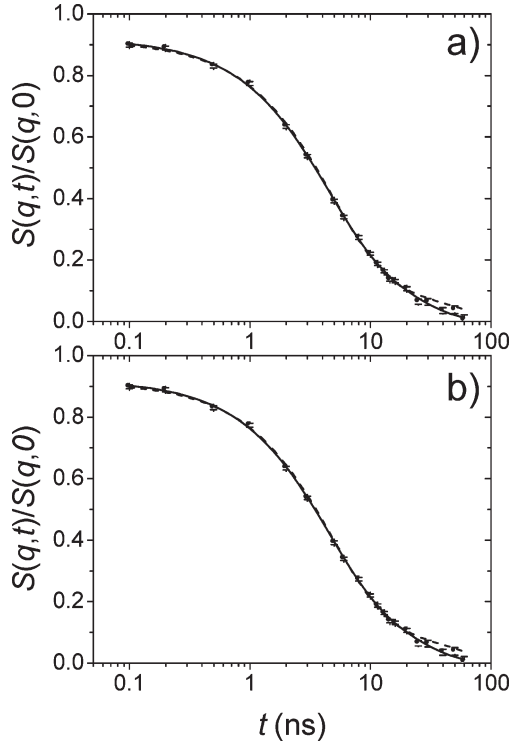

Figure 10. Fits of eq 2 (a) and eq 3 (b) to the intermediate scattering functions at 50 mg/mL measured at 24.3 °C. Solid lines: fits with $D_{micelle}$ as a free fitting parameter; dashed lines: fits with $D_{micelle}$ from DLS.

is very well recovered by both fits. This is also due to the low amplitude of the slow decay.

For higher concentrations, the determination of $D_{micelle}$ is not straightforward because the solutions are too viscous to be filtered prior to the DLS experiments. Therefore, in an alternative approach, $D_{micelle}$ was used as a free fitting parameter at 50 mg/mL, and the effect on the fit of the fast decay was examined. The resulting fits are shown in Figure 10 as well. The fitting curves recover the experimental data at high Fourier times very well; i.e., the decays are steeper with higher $D_{micelle}$ values than the ones obtained from DLS. The resulting $D_{micelle}$ values correspond to hydrodynamic micellar radii which are a factor of ~2 too small. The origin of the discrepancy may lie in a different weighting of the DLS experiment (weight-average) and the NSE experiment (number-average) over the distribution of micelle sizes. The vastly different q values where DLS and NSE experiments are carried out may also play a role. However, for both equations and for both ways of treating $D_{micelle}$, the fits are equally good in the range of the fast decay, which is due to the segmental dynamics. Therefore, we use $D_{micelle}$ as a fitting parameter for all curves, even though it leads to an increase of the uncertainties of the remaining fitting parameters.

The resulting relaxation rates $\Gamma_{internal}$ are plotted as a function of q^2 in Figure 11. For both measurements, the proportionality is obeyed for the values obtained from the decoupled model (eq 2), which indicates that the process observed is due to the breathing mode of the PNIPAM shell. Thus, the grafting density is sufficiently high, and the breathing mode dominates over the single-chain dynamics. The uncertainties of the relaxation rates from the coupled model are too high to draw a significant conclusion, and the values are therefore not shown.

The average segmental diffusion coefficients $D_{internal}$ resulting from fitting eq 2 (decoupled case) are given for all three concentrations as a function of temperature in Figure 12. Fitting eq 3 leads to similar results, however, with much higher

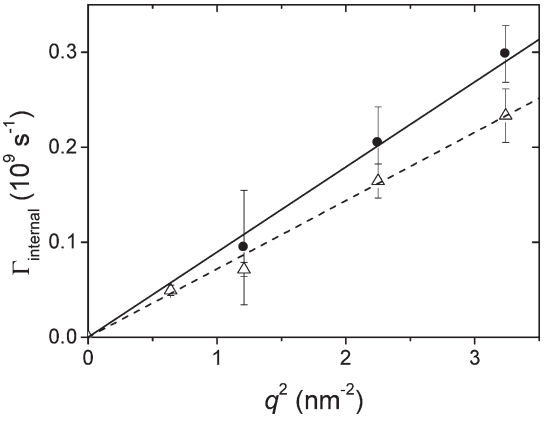

Figure 11. Relaxation rates of the segmental dynamics, $\Gamma_{internal}$, as a function of q^2. The values were obtained using eq 2. Filled circles: experimental data at 200 mg/mL at 24.4 °C; full line: linear fit. Open triangles: experimental data at 300 mg/mL at 28.6 °C; dashed line: linear fit.

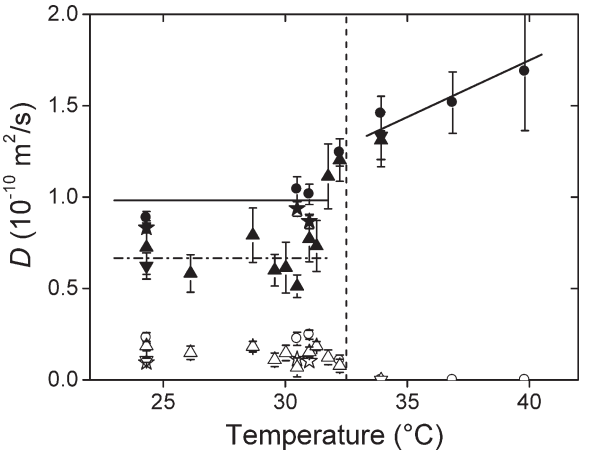

Figure 12. Temperature dependence of diffusion coefficients obtained from the fits of eq 2: stars, 50 mg/mL with $D_{micelle}$ from DLS; circles, 50 mg/mL with $D_{micelle}$ fitted; triangles up, 200 mg/mL with $D_{micelle}$ fitted; triangles down, 200 mg/mL with $D_{micelle}$ fitted; filled symbols, $D_{internal}$; open symbols, $D_{micelle}$. The vertical dashed line indicates the LCST from SANS. The horizontal full and dashed lines are the average values of 50 and 200 mg/mL below the LCST.

scatter. Figure 12 shows that the values of $D_{internal}$ are slightly lower when $D_{micelle}$ from DLS is used as a fixed fitting parameter; however, this effect is within the uncertainty. Below the collapse temperature, the values of $D_{internal}$ are not temperature-dependent within the uncertainties. The average value of $D_{internal}$ decreases with increasing polymer concentration, as expected from the increase in local PNIPAM concentration due to overlap of the micellar shells. All values are of the same order of magnitude as the ones obtained for the shell dynamics of chemically different diblock copolymer micelles in solution.[64,65]

Above the collapse temperature determined from SANS, the segmental diffusion coefficients are higher than below and do not depend on polymer concentration any longer. This seems counterintuitive since the swollen PNIPAM shell collapses and forms a melt layer around the PS core, which would imply slower dynamics. We attribute this unexpected behavior to the following mechanism: The NSE experiment measures a diffusion coefficient which is averaged over all PNIPAM segments. We assume that a gradient of diffusion coefficients exists for the segments close to the core and those further away, which are surrounded by solvent. Below the collapse temperature, the mobility of most segments is in

the time window of NSE, and we obtain an average value of the segmental dynamics in the micellar shell. In contrast, above the collapse temperature, most of the segments collapse and form a relatively immobile PNIPAM melt with only few PNIPAM blocks sticking out into the solution. Some of these blocks may bridge two micelles. Only those very mobile segments are monitored in the experiment, resulting in an average diffusion coefficient higher than in the swollen state. We conclude that NSE reveals the concentration dependence of the PNIPAM segmental dynamics and its (significant) changes at the collapse transition.

4. Conclusion

Combining several analytical methods, namely turbidimetry, fluorescence correlation spectroscopy, dynamic light scattering, small-angle neutron scattering, and neutron spin-echo spectroscopy, we have investigated thermoresponsive PS-*b*-PNIPAM-*b*-PS triblock copolymers in aqueous solution in a wide concentration range, focusing on the micelle formation, the collapse transition, and the resulting changes of the mesoscopic structure. Moreover, the segmental dynamics was probed. Detailed investigations were possible due to the use of fully deuterated PS blocks and contrast matching in neutron scattering and spectroscopy. The samples were directly soluble in water, facilitating the preparation of the solutions.

The triblock copolymers investigated in this work differ from the previously studied PS-*b*-PNIPAM diblock copolymers in two respects which reflect the bridging between micelles: (i) The micelles formed by triblock copolymers form clusters right after the collapse temperature is crossed, and no single collapsed micelles are observed. (ii) Correlation between the micelles is already present below the collapse temperature.

As compared to the literature, our triblock copolymers have relatively short hydrophobic end blocks. Thus, the investigated system is in-between the previously studied telechelic PNIPAM homopolymers and the PS-*b*-PNIPAM-*b*-PS triblock copolymers with longer PS blocks. As a consequence, the PS cores of the micelles are very small, and these micelles form small and presumably rapidly reacting building blocks of a thermoresponsive network.

Acknowledgment. We thank W. Doster and A.-K. Sommer for assistance with the DLS experiments and fruitful discussions. We kindly acknowledge given beam time by the Jülich Centre for Neutron Science at FRM II. This work was supported by the DFG priority program SPP1259 "Intelligente Hydrogele" (Pa771/4, Mu1487/8, La611/7, He2995/2-2). A.M.B.-K. gratefully acknowledges a personal grant from Deutscher Akademischer Austauschdienst (DAAD).

References and Notes

(1) Das, M.; Zhong, H.; Kumacheva, E. *Annu. Rev. Mater. Res.* **2002**, *36*, 117–311.
(2) Karg, M.; Hellweg, T. *Curr. Opin. Colloid Interface Sci.* **2009**, *14*, 438–450.
(3) Hoffman, A. S. *J. Controlled Release* **1987**, *6*, 297–305.
(4) Coughlan, D. C.; Quilty, F. P.; Corrigan, O. I. *J. Controlled Release* **2004**, *98*, 97–114.
(5) Schmaljohann, D. *Adv. Drug Delivery Rev.* **2006**, *58*, 1655–1670.
(6) Feil, H.; Bae, Y. H.; Feijen, J.; Kim, S. W. *J. Membr. Sci.* **1991**, *64*, 283–294.
(7) Park, Y. S.; Ito, Y.; Imanishi, Y. *Langmuir* **1998**, *14*, 910–914.
(8) Nykänen, A.; Nuopponen, M.; Laukkanen, A.; Hirvonen, S.-P.; Rytelä, M.; Turunen, O.; Tenhu, H.; Mezzenga, R.; Ikkala, O.; Ruokolainen, J. *Macromolecules* **2007**, *40*, 5827–5834.
(9) Schild, H. G. *Prog. Polym. Sci.* **1992**, *17*, 163–249.
(10) Lin, S.-Y.; Chen, K.-S.; Run-Chu, L. *Polymer* **1999**, *40*, 2619–2624.
(11) Katsumoto, Y.; Tanaka, T.; Sato, H.; Ozaki, Y. *J. Phys. Chem. A* **2002**, *106*, 3429–3435.
(12) Okada, Y.; Tanaka, F. *Macromolecules* **2005**, *38*, 4465–4471.
(13) Hirokawa, Y.; Tanaka, T.; Matsuo, E. S. *J. Chem. Phys.* **1984**, *81*, 6379–6380.
(14) Shibayama, M.; Tanaka, T.; Han, C. C. *J. Chem. Phys.* **1992**, *97*, 6829–6841.
(15) Liao, G.; Xie, Y.; Ludwig, K. F., Jr.; Bansil, R.; Gallagher, P. *Phys. Rev. E* **1999**, *60*, 4473–4481.
(16) Pelton, R. H.; Chibante, P. *Colloids Surf.* **1986**, *20*, 247–256.
(17) Hellweg, T.; Kratz, K.; Pouget, S.; Eimer, W. *Colloids Surf., A* **2002**, *202*, 223–232.
(18) Stieger, M.; Pedersen, J. S.; Lindner, P.; Richtering, W. *Langmuir* **2004**, *20*, 7283–7292.
(19) Höfl, S.; Zitzler, L.; Hellweg, T.; Herminghaus, S.; Mugele, F. *Polymer* **2007**, *48*, 245–254.
(20) Dingenouts, N.; Norhausen, C.; Ballauff, M. *Macromolecules* **1998**, *31*, 8912–8917.
(21) Hellweg, T.; Dewhurst, C. D.; Eimer, W.; Kratz, K. *Langmuir* **2004**, *20*, 4330–4335.
(22) Anderson, M.; Hietala, S.; Tenhu, H.; Maunu, S. L. *Colloid Polym. Sci.* **2006**, *284*, 1255–1263.
(23) Berndt, I.; Pedersen, J. S.; Richtering, W. *Angew. Chem., Int. Ed.* **2006**, *45*, 1737–1741.
(24) Kujawa, P.; Watanabe, H.; Tanaka, F.; Winnik, F. M. *Eur. Phys. J. E* **2005**, *17*, 129–137.
(25) Wang, W.; Troll, K.; Kaune, G.; Metwalli, E.; Ruderer, M.; Skrabania, K.; Laschewsky, A.; Roth, S. V.; Papadakis, C. M.; Müller-Buschbaum, P. *Macromolecules* **2008**, *41*, 3209–3218.
(26) Koga, T.; Tanaka, F.; Motokawa, R.; Koizumi, S.; Winnik, F. M. *Macromolecules* **2008**, *41*, 9413–9422.
(27) Nuopponen, M.; Ojala, J.; Tenhu, H. *Polymer* **2004**, *45*, 3643–3650.
(28) Mertoglu, M.; Garnier, S.; Laschewsky, A.; Skrabania, K.; Storsberg, J. *Polymer* **2005**, *46*, 7726–7740.
(29) Zhang, W.; Zhou, X.; Li, H.; Fang, Y.; Zhang, G. *Macromolecules* **2005**, *38*, 909–914.
(30) Tang, T.; Castelletto, V.; Parras, P.; Hamley, I. W.; King, S. M.; Roy, D.; Perrier, S.; Hoogenboom, R.; Schubert, U. S. *Macromol. Chem. Phys.* **2006**, *207*, 1718–1726.
(31) Zhou, X.; Ye, X.; Zhang, G. *J. Phys. Chem. B* **2007**, *111*, 5111–5115.
(32) Kirkland, S. E.; Hensarling, R. M.; McConaughty, S. D.; Guo, Y.; Jarrett, W. L.; McCormick, C. L. *Biomacromolecules* **2008**, *9*, 481–486.
(33) Troll, K.; Kulkarni, A.; Wang, W.; Darko, C.; Bivigou Koumba, A. M.; Laschewsky, A.; Müller-Buschbaum, P.; Papadakis, C. M. *Colloid Polym. Sci.* **2008**, *286*, 1079–1092.
(34) Bivigou-Koumba, A. M.; Kristen, J.; Laschewsky, A.; Müller-Buschbaum, P.; Papadakis, C. M. *Macromol. Chem. Phys.* **2009**, *210*, 565–578.
(35) Jain, A.; Kulkarni, A.; Bivigou Koumba, A. M.; Wang, W.; Busch, P.; Laschewsky, A.; Müller-Buschbaum, P.; Papadakis, C. M. *Macromol. Symp.*, in press.
(36) Bivigou-Koumba, A. M.; Görnitz, E.; Laschewsky, A.; Müller-Buschbaum, P.; Papadakis, C. M. *Colloid Polym. Sci.* **2010**, *288*, DOI: 10.1007s00396-009-2179-9.
(37) Nykänen, A.; Nuopponen, M.; Hiekkataipale, P.; Hirvonen, S.-P.; Soininen, A.; Tenhu, H.; Ikkala, O.; Mezzenga, R.; Ruokolainen, J. *Macromolecules* **2008**, *41*, 3243–3239.
(38) Wang, W.; Metwalli, E.; Perlich, J.; Troll, K.; Papadakis, C. M.; Cubitt, R.; Müller-Buschbaum, P. *Macromol. Rapid Commun.* **2009**, *30*, 114–119.
(39) Moad, G.; Rizzardo, E.; Thang, S. H. *Acc. Chem. Res.* **2008**, *41*, 1133–1142.
(40) Jakeš, J. *Collect. Czech. Chem. Commun.* **1995**, *60*, 1781–1791.
(41) Engels, R.; Clemens, U.; Kemmerling, G.; Nöldgen, H.; Schelten, J. *Nucl. Instrum. Methods Phys. Res., Sect. A* **2009**, *604*, 147–149.
(42) These samples were erroneously labeled 170 mg/mL in ref 35.
(43) Heskins, M.; Guillet, J. E. *J. Macromol. Sci., Part A* **1968**, *2*, 1441–1455.
(44) Förster, S.; Burger, C. *Macromolecules* **1998**, *31*, 879–891.
(45) Monkenbusch, M.; Schätzler, R.; Richter, D. *Nucl. Instrum. Methods Phys. Res.* **1997**, *A399*, 301–323.
(46) Holderer, O.; Monkenbusch, M.; Schätzler, R.; Kleines, H.; Westerhausen, W.; Richter, D. *Meas. Sci. Technol.* **2008**, *19*, 034022.
(47) Souaille, M.; Fischer, H. *Macromolecules* **2002**, *35*, 248–261.
(48) Pallares, J.; Jaramillo-Soto, G.; Flores-Cataña, C.; Vivaldo Lima, E.; Lona, L. M. F.; Penlidis, A. *J. Macromol. Sci., Part A: Pure Appl. Chem.* **2006**, *43*, 1293–1322.
(49) Bhutto, A. A. *J. Res. Sci.* **2003**, *14*, 261–269.

(50) Larque, A. M.; Maire, C.; Belissent, H.; Galin, M.; Galin, J. C. *Actual. Chim.* **199**, 187–193.
(51) Bonné, T. B.; Lüdtke, K.; Jordan, R.; Štěpánek, P.; Papadakis, C. M. *Colloid Polym. Sci.* **2004**, *282*, 833–843.
(52) Bonné, T. B.; Lüdtke, K.; Jordan, R.; Papadakis, C. M. *Macromol. Chem. Phys.* **2007**, *208*, 1402–1408.
(53) Bonné, T. B.; Lüdtke, K.; Jordan, R.; Papadakis, C. M. *Colloid Polym. Sci.* **2007**, *285*, 491–497.
(54) Procházka, K.; Limpouchoá, Z.; Webber, S. E. In Salamone, J. A., Ed.; *Polymeric Materials Encyclopedia*; CRC Press: Boca Raton, FL, 1996; Vol. *1A,B*; pp 764−772.
(55) Schuch, H.; Klingler, J.; Rossmanith, P.; Frechen, T.; Gerst, M.; Feldthusen, J.; Müller, A. H. E. *Macromolecules* **2000**, *33*, 1734–1740.
(56) Semenov, A. N.; Joanny, J.-F.; Khokhlov, A. R. *Macromolecules* **1995**, *28*, 1066–1075.
(57) Kujawa, P.; Segui, F.; Shaban, S.; Diab, C.; Okada, Y.; Tanaka, F.; Winnik, F. M. *Macromolecules* **2006**, *39*, 341–348.
(58) Nojima, R.; Sato, T.; Qiu, X.; Winnik, F. M. *Macromolecules* **2008**, *41*, 292–294.
(59) Wang, W.; Metwalli, E.; Perlich, J.; Papadakis, C. M.; Cubitt, R.; Müller-Buschbaum, P. *Macromolecules* **2009**, *42*, 9041–9051.
(60) Grimson, M. J. *J. Chem. Soc.* **1983**, *79*, 817–832.
(61) Shibayama, M.; Tanaka, T.; Han, C. C. *J. Chem. Phys.* **1992**, *97*, 6829–6841.
(62) Ewen, B.; Richter, D. *Adv. Polym. Sci.* **1997**, *134*, 1–129.
(63) Kanaya, T.; Monkenbusch, M.; Watanabe, H.; Nagao, M.; Richter, D. *J. Chem. Phys.* **2005**, *122*, 144905.
(64) Matsuoka, H.; Yamamoto, Y.; Nakano, M.; Endo, H.; Yamaoka, H.; Zorn, R.; Monkenbusch, M.; Richter, D.; Seto, H.; Kawabata, Y.; Nagao, M. *Langmuir* **2000**, *16*, 9177–9185.
(65) Castelletto, V.; Hamley, I. W.; Yang, Z.; Haeussler, W. *J. Chem. Phys.* **2003**, *119*, 8158–8161.
(66) Yardimci, H.; Chung, B.; Harden, J. L.; Leheny, R. L. *J. Chem. Phys.* **2005**, *123*, 244908.